research papers

Phase imaging using time-of-flight neutron diffraction

M. J. Gutmann,[a]* W. Kockelmann,[a] L. C. Chapon[a] and P. G. Radaelli[a,b]

[a]Rutherford Appleton Laboratory, ISIS Facility, Chilton Didcot, Oxfordshire OX11 0QX, UK, and [b]Department of Physics and Astronomy, University College London, Gower Street, London WC1E 6BT, UK. Correspondence e-mail: m.j.gutmann@rl.ac.uk

A technique that allows the spatial distribution of crystallographic phases in the interior of an object to be reconstructed from neutron time-of-flight (TOF) diffraction is described. To this end, the shift of the Bragg peaks due to the so-called 'geometrical aberration' is exploited. A collimated incident white beam is used to perform a translational or rotational scan of the object whilst collecting a TOF data set for each sample position or orientation. Depending on the location of any scattering material along the line of the incident beam path through the object, the measured d-spacings of the corresponding Bragg peaks are shifted with respect to their nominal values, which are attained only at the geometrical centre of the instrument. Using a formula that is usually employed to correct for sample offset, the phase distribution along the incident beamline can be directly reconstructed, without the need to perform a tomographic reconstruction. Results are shown from a demonstration experiment carried out on a cylindrical Al container enclosing an arrangement of Cu and Fe rods. On the basis of this formalism, an optimized experimental geometry is described and the potential and limits of this technique are explored, as are its applicability to X-ray and constant-wavelength neutron diffraction.

1. Introduction

Techniques for non-destructive testing of materials using X-ray and neutron radiation find widespread application in those fields of natural sciences where sampling is often restricted or impractical, such as engineering, geology and archaeology. Neutrons and X-rays are, to a large extent, complementary with respect to scattering contrast and penetration depth. While X-rays are more sensitive to heavier than to lighter elements, there is no such general tendency for neutrons. Unless they are extremely energetic, X-rays are absorbed within the first millimetre of the material and are therefore ideal for surface studies. Neutrons on the other hand are often an indispensable probe for obtaining information from the interior of a centimetre-thick engineering piece or a unique museum object.

Non-destructive techniques are of particular interest for mapping a given physical or structural parameter, for instance, the elemental composition or the strain field. For example, micro-focus X-ray fluorescence and diffraction imaging with synchrotron radiation provide information on surface elements and phases, respectively. Neutron diffraction is capable of measuring elastic strains in the bulk of extended engineering components (Allen *et al.*, 1985; Dann *et al.*, 2003). Conventional X-ray and neutron radiographic and tomographic imaging, which exploits the attenuation contrast in materials, find widespread use in engineering and archae-

ometry (Schillinger *et al.*, 2000; Deschler-Erb *et al.*, 2004). More recent tomographic techniques include the use of phase contrast techniques using scattered X-rays (Chapman *et al.*, 1997) and neutrons (Allman *et al.*, 2000). Measurements of the refractive index distribution and, simultaneously, of the attenuation coefficient reveal detailed images of the interior of objects where the traditional tomographies fail (Treimer *et al.*, 2003).

X-ray and neutron imaging methodologies and experimental capabilities are rapidly developing, with the advent of new intense synchrotron and neutron sources. Among the conventional X-ray radiography and tomography techniques, and the closely related techniques employing neutron beams, methods that produce element- or phase-selective three-dimensional maps are particularly interesting. There are essentially three approaches to achieve this, depending on the signal used to reconstruct the phase or compositional maps; this signal can be extracted from the direct beam (transmission), from the scattered beam (diffraction) or from some form of beam-induced radiation (emission). Transmission techniques, essentially modifications of conventional radiography/tomography, are fast, since the full object can be simultaneously illuminated. Therefore, each exposure contains a two-dimensional encoding of the sample. The disadvantage of transmission techniques is the poor sensitivity to minority phases/elements. For example, an image can be reconstructed by comparing the on-resonance and off-reso-

nance epithermal-neutron absorption of individual isotopes (Kamiyama *et al.*, 2005). Likewise, maps of crystallographic phase distribution can be obtained in transmission mode by employing Bragg edges as an imaging signal (Santisteban *et al.*, 2001). With a suitable two-dimensional detector and a parallel neutron beam, complete isotope- or phase-resolved radiographies can be obtained with a single exposure, and images taken at various sample orientations can be combined to form a three-dimensional tomogram of an object.

By contrast, diffraction and emission techniques are slower, since they employ a 'pencil' beam (zero-dimensional encoding), but are, in principle, more sensitive to minority components. For example, it is in principle possible to construct an isotope-resolved radiographic map by scanning a pencil beam and monitoring the prompt gamma emission (thermal neutrons) or the gamma emission following neutron resonant capture (epithermal neutrons).

It would be highly desirable to combine crystallographic phase analysis, as distinct from chemical composition analysis, with imaging. Phase identification and determination of the spatial distribution of phases would be of value, for example, in bulk rock of unknown mineral composition and for unique archaeological materials for which any sampling is unacceptable. Neutrons combine the non-destructive nature of the analysis technique with the possibility to study bulky extended samples. In principle, maps of crystallographic phase distribution can be obtained by conventional diffraction, which has intrinsically zero-dimensional encoding and requires a 'pencil' beam. Direct point-by-point phase maps can be obtained by employing tight radial collimation of the scattered beam, in analogy with what is routinely done to measure residual strains. For example, the phase composition of bulky samples can be derived from high-energy energy-dispersive X-ray scans with a narrow beam, achieving a submillimetre spatial resolution (Colston *et al.*, 2000). Owing to the inherently high intensity, X-ray measurement times can be kept short, of the order of a few minutes per scan. Energy-dispersive TOF diffraction was used to produce a one-dimensional scan of a diffracting volume of $2 \times 2 \times 2$ mm through the thickness of an archaeological bronze object (Siano *et al.*, 2006). However, detailed three-dimensional maps from point-by-point neutron diffraction are unlikely to be produced on a regular basis owing to flux limitations. In the absence of secondary beam collimation, two-dimensional maps are produced, in which the phase distribution along the beam direction is averaged, with an appropriate weight due to absorption. Combining many scans illuminating the sample from different angles can be used to reconstruct three-dimensional images carrying information on the phase composition.

We propose here a new diffraction imaging technique, based on TOF neutron diffraction, with intrinsic one-dimensional encoding, which is more than an order of magnitude faster than existing diffraction-based techniques. The position of the scattering centres along the line of the beam is encoded in the shape and position of the Bragg peaks, through what is normally known as the geometrical aberration effect. We derive the master equations describing this technique, and on this basis, we define the optimal instrument geometry. The feasibility of the technique on existing instrumentation is demonstrated by producing the image of an Al cylinder with Cu and steel rods inside. Finally, we explore how this technique could be extended to steady-state neutron and high-energy X-ray diffraction.

The paper is organized as follows. The theory underpinning image reconstruction from peak shape and position, including the real-space resolution, is developed in §§2–4. §5 describes the sample and setup used in the experiment. The results are shown in §6. In §§7 and 8, we discuss a data analysis strategy and an extension of the method to high-energy X-rays and steady-state neutron sources; this is followed by a discussion and an overall summary.

2. Effect of sample displacement in a TOF neutron powder diffractometer

TOF neutron powder diffractometers at spallation neutron sources such as GEM at ISIS (Day *et al.*, 2004) employ large detector arrays for efficient data collection. The detectors are usually grouped into banks and the data focused in *d*-spacing to a nominal scattering angle for each bank. The resulting one-dimensional diffraction patterns are then typically used as independent data sets in a multi-bank refinement. In this 'open' geometry, the scattering angle 2θ is defined by two lines connecting the 'scattering centre' of the sample with the middle of the source and with the detector, and naturally depends on the sample position. The 'effective' detector positions are calibrated with a crystalline standard, which also defines the 'ideal' sample position. A displacement of the sample from this ideal position will result in an aberration, whereby different lattice parameters are measured in different banks, unless this is corrected for during the structural refinement. The correction can be calculated in terms of the two components of the sample displacement, along the incident beam and perpendicular to the beam. This process has been discussed in some detail by Wang *et al.* (2002) in the approximation of small sample displacements.

In our case, only the displacement of the sample along the incident 'pencil' beam is relevant, but dealing with bulky extended samples, we will develop the second-order correction to the small sample displacement formula. Fig. 1 illustrates the geometry for longitudinal sample displacements.
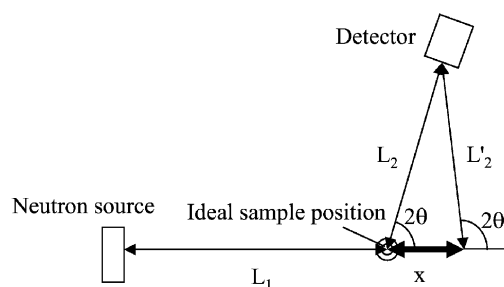
Figure 1
Geometry for a sample displacement along the incident beam.

The modified scattering angle θ' can be expressed in terms of sample displacement, x, primary and secondary flight paths L_1 and L_2, respectively, and ideal scattering angle θ as follows:

$$\sin\theta' = \sin\left(\theta + \frac{1}{2}\arcsin\left\{\frac{r\sin(2\theta)}{[1+r^2-2r\cos(2\theta)]^{1/2}}\right\}\right). \quad (1)$$

Here, $r = x/L_2$. Similarly, the modified total flight path is obtained as

$$L'_{\text{tot}} = L_2\left\{r + \left[1 + r^2 - 2r\cos(2\theta)\right]^{1/2}\right\} + L_1. \quad (2)$$

The nominal time-of-flight in microseconds of a neutron of a given wavelength for a sample at the ideal position ($x = 0$) is derived from Braggs law:

$$t_0 = 505.5d(L_1 + L_2)\sin\theta, \quad (3)$$

where d is the d-spacing in ångströms and the flight paths are in metres. An analogous expression is obtained for the shifted TOF t'. Equations (1)–(3) are exact; after collecting all the terms in (1)–(3) and performing a Taylor series expansion around the ideal sample position, i.e. $r = 0$, the relative shift in TOF defined by $\Delta t/t = (t' - t_0)/t_0$ is obtained as

$$\frac{\Delta t}{t} = (x/L_2)\left\{\frac{L_2[1-\cos(2\theta)]}{L_1 + L_2} + \cos^2\theta\right\} + (x/L_2)^2$$
$$\times \frac{1}{2}\left(\frac{\cos^2\theta}{L_1 + L_2}\right)\left[3(L_2 - L_1)\sin^2\theta + 2(L_2 + L_1\cos^2\theta)\right]$$
$$+ O\left[(x/L_2)^3\right]. \quad (4)$$

The above formula can generally be used to correct for the effect of sample displacement along the incident beam leading to consistent lattice parameters for all banks. This correction is usually made only up to the linear term in x since higher-order terms are negligible. Note that the term linear in x/L_2 is identical to equation (6) of Wang et al. (2002):

$$\frac{\Delta t}{t} = x\kappa,$$
$$\kappa = \frac{[1-\cos(2\theta)]}{L_1 + L_2} + \frac{\cos^2\theta}{L_2}. \quad (5)$$

Equations (4) and (5) can be easily inverted to solve for the sample displacement, x, given all the other quantities. Note that the information about the sample position is encoded in the Bragg peaks and is therefore phase-dependent. Let us now consider the experimental geometry described in Fig. 1, and let us first assume that each of the constituent phases of the extended object occurs in a 'lump', which is small with respect to the overall size of the object. An example of this would be that of small crystalline inclusions in an amorphous matrix. In this case, each of the lumps, once hit by the beam, will produce a set of distinct Bragg peaks, and their displacements from the 'ideal' d-spacing will measure the displacement of the lump along the direction of the pencil beam. By scanning the object vertically and laterally across the beam, one can build a full three-dimensional map of the position of the inclusions within the object. A slightly more complex case is that of crystalline phases extending over a large part of the sample. In this case,

the peak shape will reflect the distribution of each phase: for example, an extended phase with a hole in it will produce a 'top-hat' peak with a dip corresponding to the position of the hole.

3. Instrument geometry and its effect on spatial resolution

Having established the general principles of this technique, the next step is to define the parameters controlling its real-space resolution. The transverse resolution (i.e. perpendicular to the beam) is straightforwardly related to the size and divergence of the beam itself and can be optimized in a manner similar to that routinely performed for residual strain measurements. Deriving the longitudinal resolution (i.e. along the beam), is somewhat less straightforward, and we will discuss this process in some detail. As we have seen, the position and spatial extent of each crystalline phase is encoded in the shape and position of the Bragg peaks; therefore, all other sources of peak broadening, such as intrinsic instrument resolution and strain, define the minimum extent of the imaged features in the longitudinal direction. The various components of the longitudinal resolution ('blurring') due to TOF pulse shape, detector pixel size and beam divergence can be easily estimated in the linear approximation using equation (5) and the usual TOF instrument resolution formulae (Willis, 1994):

$$B_{\text{pulse}} \simeq \frac{1}{\kappa}\left(\frac{\Delta t}{t}\right)_{\text{pulse}}, \quad (6)$$

$$B_{\text{pixel}} = \frac{1}{\kappa}\cot\theta\left(\frac{w_{\text{pix}}}{2L_2}\right), \quad (7)$$

$$B_{\text{div}} \simeq \frac{1}{\kappa}\cot\theta\left(\frac{w_{\text{mod}}}{2L_1}\right). \quad (8)$$

w_{pix} and w_{mod} are the width of a detector pixel and the moderator, respectively. The total real-space blurring can be well modelled by adding equations (6)–(8) in quadrature. From equation (7), one deduces that the pixel width sets a lower limit to the longitudinal resolution. B_{pulse} and B_{div} are proportional to L_2, so a short secondary flight-path appears to be an advantage. However, a very short L_2 would widely separate Bragg peaks generated at opposite ends of the sample, making the diffraction pattern completely unrecognizable, and would make the linear approximation invalid [this effect can be quantitatively assessed with equation (4)]. A good compromise is for L_2 to be 4–5 times larger than the typical sample diameter.

The parameters for the instrument used in the demonstration experiment (see below) are $(\Delta t/t)_{\text{pulse}} = 0.005$, $w_{\text{pix}} = 3$ mm, $w_{\text{mod}} = 0.1$ m, $L_1 = 8.3$ m and $L_2 = 0.27$ m.

For these parameters, the various contributions are shown in Fig. 2. The best longitudinal resolution is obtained for a scattering angle close to $2\theta = 90°$ and amounts to slightly less than 5 mm. Also, the quadratic correction in equation (4)
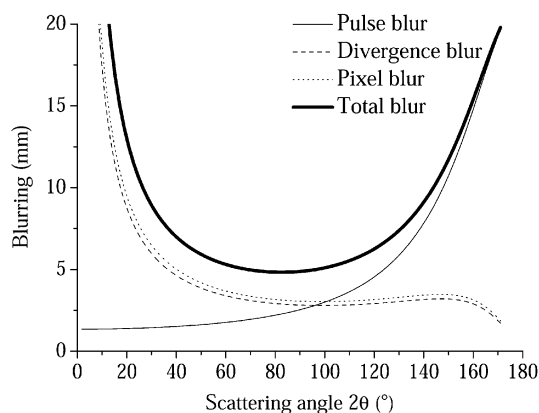
Figure 2
Expected spatial resolution for $(\Delta t/t)_{pulse} = 0.005$, $w_{pix} = 3$ mm, $w_{mod} = 0.1$ m, $L_1 = 8.3$ m and $L_2 = 0.27$ m. The blurring arising from the pixel resolution and divergence are comparable in magnitude for this parameter set and have the same angular dependence.
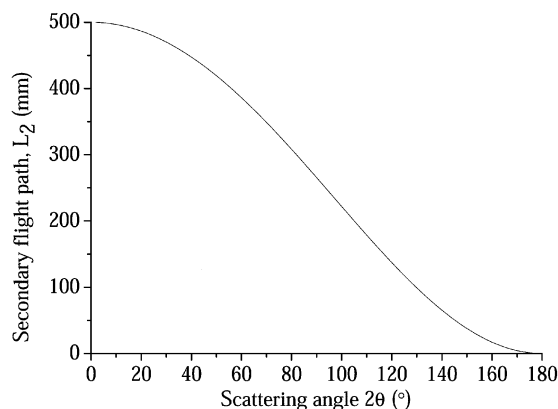

Figure 3
Detector locus corresponding to the negative sign of the square root term in equation (10) for $L_1 = 8300$ mm and $\kappa = 0.002$. For backscattering ($2\theta = 180°$) $L_2 = 0$ for constant κ.

Figure 4
Detector inclination in degrees *versus* scattering angle using the same parameters as for Fig. 3. An inclination angle of zero means that the detector is parallel to the beam. A positive (negative) inclination indicates that the detector is tilted toward the incident (transmitted) beam. The strong variation near 120° corresponds to an inflection point in the detector locus shown in Fig. 3 (at this point, the detector is normal to the beam).

amounts to only 4% of the linear term, so that the linear approximation is justified. We remark in passing that, for an instrument with a long primary but short secondary flight path, the term involving L_1 may be neglected near 90°. This omission leads to a particularly simple expression for the relative shift in TOF and sample displacement:

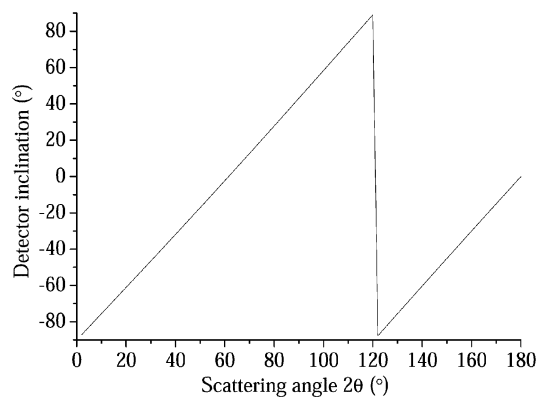$$\Delta t/t \simeq x\cos^2\theta/L_2(\theta). \qquad (9)$$

The largest contributions to the longitudinal 'blurring' are from the pixel size and beam divergence and are about equal in our case. With smaller pixels, a less divergent beam and a somewhat longer primary flight path [to reduce further the pulse term of equation (6)], a resolution of 1–2 mm can be easily obtained, albeit at the expense of flux.

4. Optimization of the detector locus

A cursory consideration of possible data analysis strategies for this technique outlines a further issue to be resolved. In conventional TOF powder diffractometry, data from individual detectors are 'focused' over a large angular range, by adding together data bins with the same d-spacings. However, from equation (5) one easily deduces that this method is not adequate. In fact, for a generic detector locus (for example, at constant L_2), the conversion factor κ between peak shift and sample displacement is angle dependent, and adding together data from different angles would result in further real-space broadening. In principle, data could be added together in small angular domains and the resulting multiple histograms processed separately. This strategy was adopted in our test experiment, but this fine subdivision is at the expense of the single-pattern statistics, which ultimately limits the speed of the data collection. Alternatively, the d-spacing ranges around given Bragg peaks could be rescaled according to equation (5) before focusing, but this is only possible for well separated peaks. Therefore, it would be extremely desirable to define a detector locus over which κ does not vary. The condition to

define the detector locus is then given by $\kappa =$ constant and results from inverting equation (5):

$$L_2(\theta) = -1/(2\kappa)\big[\cos^2\theta - 2 + \kappa L_1 \pm (\cos^4\theta - 4\cos^2\theta$$
$$+ 6\kappa L_1\cos^2\theta + 4 - 4\kappa L_1 + \kappa^2 L_1^2)^{1/2}\big], \qquad (10)$$

where only the solution leading to a positive L_2 is admissible. The resulting detector locus is shown in Fig. 3 for the parameters indicated in the caption.

As we have seen, only scattering angles around 90° are of interest, since they yield the best longitudinal resolution. Therefore, a good approximation to the locus defined in equation (10) could be a flat (or better, conical) detector positioned at 90° with an appropriate inclination. The value of the inclination is obtained by differentiation of equation (10):

$$x = L_2(\theta)\cos 2\theta, \qquad y = L_2(\theta)\sin(2\theta),$$
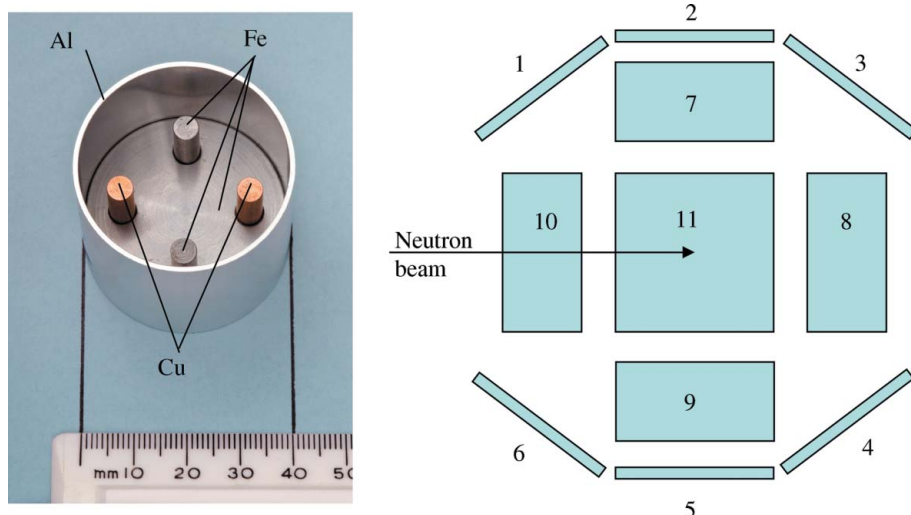$$dy/dx = \frac{dy}{d\theta}\left(\frac{dx}{d\theta}\right)^{-1}.$$

The resulting inclination as a function of scattering angle 2θ is shown in Fig. 4. Notably, for $2\theta = 90°$, the detector should be inclined at an angle close to $45°$.

By inserting equation (1) into equations (7) and (8), one finds a small variation of the real-space resolution as a function of the scattering angle. This is not in general a serious problem, and could be compensated by adjusting the pixel size w_{pix} accordingly.

5. Test experiment

In order to verify these concepts, we performed a test experiment, with the goal of imaging a thin cylindrical annular sample made of Al with a diameter and height of 40 mm, respectively, and a wall thickness of 1 mm, containing two copper rods and two steel rods in a cross-shaped arrangement. A bulk steel cylinder with four holes in a cross-shaped arrangement was placed at the bottom of the Al cylinder to support two copper and steel rods of 5 mm diameter each. For support, the rods were inserted into steel holders below and above the beam. This left a vertical gap of approximately 13 mm for the beam to go through. A photograph of the object is shown in Fig. 5.

Measurements were performed on the SXD beamline at the ISIS spallation neutron source at the Rutherford Appleton Laboratory (UK). Although SXD is primarily used for single-crystal diffraction, its short secondary flight path made it the best choice for this experiment. An *in vacuo* translation stage was not available at the time of this experiment, so the test object was suspended on a rotation stage. The axis of the cylinder was aligned with the ideal sample position of the diffractometer.

As one would expect, the SXD detectors do not follow the ideal detector locus described in §4 but are mounted at right angles to the secondary beam. SXD uses pixellated flat area detectors with 64×64 pixels per detector. Each pixel covers an area of 3×3 mm. The incident flight path is 8.3 m and the centre of each of the six equatorial plane detectors is 225 mm away from the sample. Four out-of-plane detectors are situated $45°$ below the equatorial plane, their centres being at a distance of 270 mm. A schematic detector layout is shown in Fig. 5, along with the sample used. The size of the incident beam was set to 2×2 mm. However, the SXD beam collimation is not designed to produce a beam with perfectly defined edges, and this resulted in significant transverse blurring of the image (see below).

To simplify the analysis and owing to real-space resolution considerations, only data from the banks at $90°$ were used. Vertical pixel columns with a total width of about $\pm 2°$ around $90°$ were summed and the TOF spectra were carefully aligned to avoid additional line broadening of the diffraction lines. Owing to counting statistics on the weak lines originating from Al, four images were reconstructed corresponding to scattering angles of 82, 86, 90 and $94°$, with a width of $4°$ for each scattering angle in the out-of-plane detectors labelled 7 and 9 in Fig. 5; these images were then combined to form the final reconstructed image using equation (5).

6. Results

At the beginning of the measurement, the two Cu rods were approximately aligned with the incident beam. Prior to running the experiment, the first diffraction patterns were inspected to assess the magnitude of the diffraction line shifts in TOF and also to estimate the time required to obtain sufficient statistics. We found 40 min per scan to be adequate, and thus 31 scans in steps of $6°$ were collected covering an angular range of $180°$.

The resulting diffraction patterns are shown in Fig. 6 as a contour plot. The ideal reflection positions (in TOF) of the Cu(200), Fe(110) and Al(111) lines are marked with dotted vertical lines. The lattice parameters for Cu, Fe and Al were taken as $a = 3.6149$, 2.8665 and 4.0495 Å, respectively (http://www.webelements.com/index.html). The observed diffraction lines are clearly shifted with respect to the calculated Bragg peaks of the metal structures. The shifts range between ~50 µs and ~300 µs for the groups of peaks in the analysed TOF range from 5000 to 8000 µs. It should be noted that the observed TOF spectrum contains many more peaks, available for phase identification by means of structural databases. In this test experiment, the

Figure 5
Left: Object used in the test experiment. The steel rods appear grey; the other two rods are made of Cu. The top steel cylinder used as a cover is not shown. Right: Schematic detector layout of the SXD instrument. The square in the middle corresponds to the detector at the bottom of the instrument. Four detectors are situated and inclined $45°$ below the equatorial plane and six in the equatorial plane. Each detector spans approximately $\pm 23°$ vertically and horizontally around the detector centre.

data were not corrected for the incident flux, and thus the relative intensities are not suitable for phase identification. The relative shifts, $\Delta t/t$, are of the order of 10^{-2}, *i.e.* much larger than expected from strain effects which are typically of the order 10^{-3} (Dann *et al.*, 2003).

The shifted diffraction lines in Fig. 6 are assigned as follows: Cu(200) from the two rods at about 5350 and 5700 μs, Fe(110) from the two Fe rods at about 6050 and 6300 μs, and Al(111) from the aluminium cylinder at about 6900 and 7400 μs. The lines in the 6200–6500 μs range at 0° and 180° are from Cu(111) and the lines in the 4000–4500 μs range around 90°
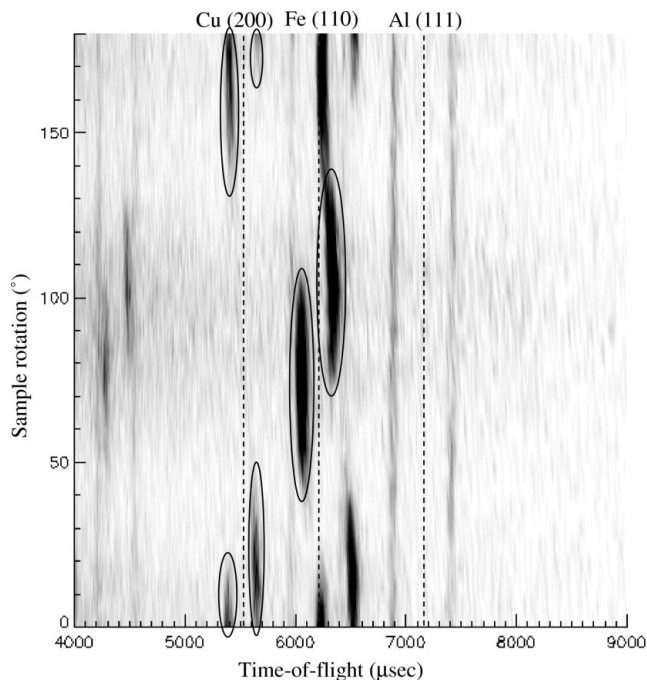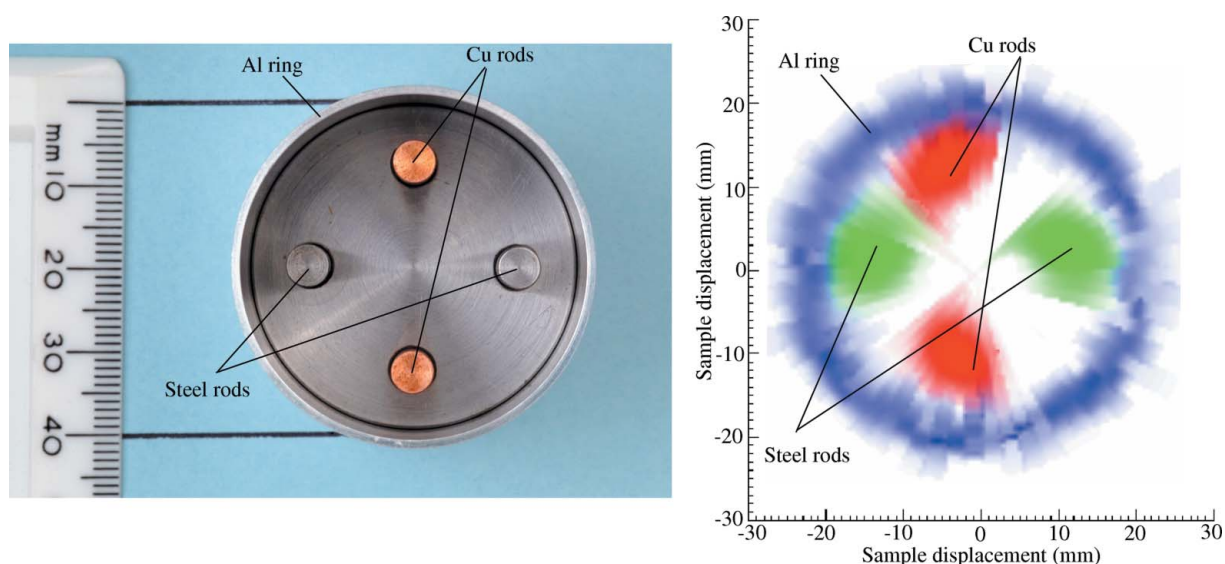

Figure 6
Diffraction intensities *versus* sample rotation angle and TOF. The expected positions of Cu(200), Fe(110) and Al(111) are drawn as vertical dashed lines.

are from Fe(200). The lines corresponding to Cu and Fe vary in intensity as a function of angle, as one expects, since the metal rods are in the beam only in a restricted angular range. The angular shift of the two rods may be ascribed to a lateral sample offset of about 3 mm, which is reproduced in the image reconstruction (see below).

For the reconstruction of the phase distribution, Gaussian profiles were fitted to extract the positions and intensities of the diffraction lines. From the positions of the Bragg lines and their assignment to the elements Cu, Fe and Al, respectively, the displacement, x, along the incident beam direction was derived using equation (5). For each crystalline phase, $\Delta t/t$ was calculated from $(t_{obs} - t_{exp})/t_{exp}$, where 'obs' and 'exp' refer to observed and expected values, respectively. For the image reconstruction the x displacements were directly transformed into a polar plot of the scanning variable, *i.e.* the sample rotation angle. The extension of a phase component along the incident beam direction, *i.e.* the chord defined by the pencil beam through each component, was determined using the width of the Gaussian peaks. Once again, using equation (5), the Gaussian profile was converted from TOF to linear displacement, x, with a truncation at twice the Gaussian variance. This procedure produced three separate images, one of each component, which were assigned distinct colour channels (red for Cu, blue for Al and green for Fe) and finally combined. The colour brightness in the reconstructed image does not reflect the phase amount in the sample, since images for each phase were scaled separately to their respective maxima. The resulting image is shown in Fig. 7, together with a photograph of the object.

The reconstructed image clearly shows an outer blue ring, representing the aluminium container, as well as four spots in a cross-shaped arrangement originating from Cu and Fe. The ring appears to exhibit striations in the vicinity of the rods. This effect merely reflects the uncertainty in extracting a reliable width and intensity when the beam was passing through the rods before hitting the Al on the back. The overall

Figure 7
Test sample from top (left) and reconstructed image (right) displayed on approximately the same length scale.

dimensions of the reconstruction and of the sample agree very well. The slight distortion of the Al ring may be attributed to the intrinsic weakness of the corresponding diffraction lines and the resulting uncertainty in the determination of the peak parameters. As for the rods, the maximum intensity is well concentrated within their 5 mm diameter and falls off rapidly outside this radius. The relative orientation of the Cu and Fe rods is consistent with a $90°$ angle, as for the sample. It should be emphasized that the experimental radial resolution matches closely the expected spatial resolution as discussed in §3. Further inspection of the centroids of the Cu and Fe rods in the reconstructed image also reveals a 3 mm lateral offset of the cylindrical axis with respect to the beam centre, thus explaining the relative angular shift of the corresponding features in the diffraction patterns in Fig. 6. Within the uncertainties of the measurement and of the analysis, a satisfactory reconstruction of the object and its interior has thus been obtained along with information on the phases contained inside.

7. Data analysis strategies

The results obtained in our test experiment could be significantly improved in a realistic situation by adopting an appropriate data analysis strategy. First of all, it is clear that the overall phase composition needs to be known in advance. This information can be gathered very rapidly on the same instrument used for tomography by measuring the diffraction pattern with a full beam in back scattering, which is where the effect of having an extended sample is minimized. Identification of phases in an extended object could also be achieved with an additional transmission detector recording the Bragg edges of the constituent phases. In addition, it is useful to know the overall shape of the object in advance, although this is not strictly necessary. The focused patterns from the $90°$ detector, or the single pattern if our 'focusing' geometry is adopted, will then be analysed by a modified Rietveld program, where the definition of the peak 'profiles' for each crystallographic phase will contain the distribution of that phase along the diffracting pencil. For this purpose, the diffracting pencil (or, if the exact shape of the sample is not known, an extended line containing it) will be subdivided into a number of bins, smaller but approximately equal to the real-space instrumental resolution. The full profile will be reconstructed by convoluting the instrumental resolution with a series of delta functions. The weights of these delta functions represent the amount of each phase in a given bin, and are the refineable parameters in the fit. A 50 mm sample at 2.5 mm resolution containing three phases corresponds to 60 parameters, which is well within the capabilities of modern Rietveld codes. Codes that rely on numerical convolution to reconstruct peak profiles should be able to implement this method in a straightforward way. This analysis can be quantitative, provided that the data are corrected for absorption and that texture is either absent or appropriately modelled. It is noteworthy that texture will be significantly averaged by a conical detector completely surrounding the sample.

8. Extension to steady-state neutron and X-ray sources

This technique can be straightforwardly extended to steady-state neutron sources (Debye–Scherrer geometry), provided that equation (5) is replaced by the well known correction formula for longitudinal displacement, which, for small displacements, is

$$\Delta 2\theta = x\kappa,$$
$$\kappa = \sin(2\theta)/R, \tag{11}$$

where R is the radius of the diffractometer, and corresponds to L_2. It is noteworthy that equation (11) can be easily derived from equation (5) in the limit of large L_1, as one would expect. Likewise, the second-order correction can be derived from equation (4) in the same limit. Because of the need to measure near $90°$, only a restricted d-spacing range would be available for each wavelength, which may limit the applicability of this method to simple metallic objects. Application to hard X-rays is more problematic: only very high-energy X-rays (> 100 keV) would be of interest here, since one needs significant penetration to take advantage of the longitudinal profiling. However, all scattering is concentrated at low angle, where the geometric conversion is less favourable. For example, from equation (7), it is easy to see that the B_{pix} is approximately 20 times larger than the pixel width for the Cu(200) reflections measured with 150 keV X-rays ($2\theta = 2.8°$). This means that a 50 μm pixel resolution would be required to obtain 1 mm spatial resolution. Further work would be required to determine whether this methodology is applicable in practice with high-energy X-rays.

9. Discussion

Our experimental results show that phase imaging based on geometrical aberrations has a potential for obtaining phase distributions and shape information of simple composite objects. The technique may be applied, for instance, to a homogeneous host material with inclusions, or an object composed of several f.c.c. metal phases, as is the case for our test sample. We note that most engineering samples belong to the latter group, as do many archaeo-metallurgical materials. Limitations with respect to achievable spatial resolution and phase contrast, phase detection limits, and ability to measure bulky samples with strongly absorbing constituents and in the presence of texture will need to be investigated further.

The imaging technique presented here can be regarded, at least, as complementary to the techniques mentioned in the introduction, with its own advantages and disadvantages. Whilst traditional imaging techniques acquire information about the sample homogeneity in the transverse beam direction, and whilst tomography relies on a complete set of absorption measurements and three-dimensional computed reconstruction algorithms, our technique gives information along the line of sight with respect to the incident beam. The position and extent of objects along this diffracting pencil can be directly reconstructed without the need for a complete set of scans.

The method, demonstrated here for a quasi-two-dimensional object (see Fig. 7), can straightforwardly be extended to three-dimensional tomography by adding a second scanning variable, along the height of the sample. Mapping crystalline phases on neutron strain scanners that use a secondary diffracted beam collimator (zero-dimensional encoding, three scanning dimensions) has advantages for phase identification in multiphase systems and for determining continuous phase distributions, but this technique is inefficient in terms of the time required for mapping and pinpointing a localized phase component. The peak aberration technique (one-dimensional encoding, two scanning dimensions) presented here has advantages for surveying an object with unknown internal structure and it is considerably faster at locating the phase component (*e.g.* an inclusion) in an otherwise homogeneous matrix.

10. Summary and conclusions

We used geometrical aberration in TOF neutron powder diffraction for mapping the phase composition in an extended sample by a rotational scan in the neutron beam. The technique is based on a formula used to correct for off-centre sample displacement. The feasibility of the method was demonstrated on a simple test sample containing objects of Cu, Fe and Al.

We presented a set of equations to derive the spatial resolution for a given experimental setup, which were found to be in good agreement with our experimental results. Based on these equations, an instrument having a natural detector locus with constant line shift in TOF is proposed. The TOF scale would serve as a fixed ruler for any object size for which the linear sample displacement formula is sufficiently accurate.

We believe that crystalline phase imaging will find immediate application in areas of cultural heritage research and of engineering, wherever non-destructive testing is required. Phase and structural mapping can constructively complement conventional attenuation contrast tomographies, which provide only indirect information on the microstructural properties of materials. Applications may include locating hidden repair parts inside valuable museum objects, and detecting metal parts (*e.g.* uranium) embedded in nontransparent materials, refuse or containers.

References

Allen, A. J., Hutchings, M. T., Windsor, C. G. & Andreani, C. (1985). *Advances in Physics*, **34**, 445–473.

Allman, B. E., McMahon, P. J., Nugent, K. A., Paganin, D., Jacobson, D. L., Arif, M. & Werner, S. A. (2000). *Nature (London)*, **408**, 158–159.

Chapman, D., Tomlinson, W., Johnston, R. E., Washburn, D., Pisano, E., Gmur, N., Zhong, Z., Menk, R., Arfelli, F. & Sayers, D. (1997). *Phys. Med. Biol.* **42**, 2015–2025.

Colston, S. L., Jupe, A. C. & Barnes, P. (2000). *Radiation in Art and Archeometry*, pp. 129–150. Amsterdam: Elsevier Science.

Dann, J., Daymond, M. R., James, J. A. J., Santisteban, J. R. & Edwards, L. (2003). *Proceedings of the ICANS-XVI*, pp. 231–238. Forschunszentrum Jülich GmbH, Jülich, Germany,

Day, P., Enderby, J. E., Williams, W. G., Chapon, L. C., Hannon, A. C., Radaelli, P. G. & Soper, A. K. (2004). *Neutron News*, **15**, 19.

Deschler-Erb, E., Lehmann, E. H., Pernet, L., Vontobel, P. & Hartmann, S. (2004). *Archeometry*, **46**, 647–661.

Kamiyama, T., Ito, J., Noda, H., Iwasa, H., Kiyanagi, Y. & Ikeda, S. (2005). *Nucl. Instrum. Methods Phys. Res. Sect. A*, **542**, 258–263.

Santisteban, J. R., Edwards, L., Steuwer, A. & Withers, P. J. (2001). *J. Appl. Cryst.* **34**, 289–297.

Schillinger, B., Lehmann, E. & Vontobel, P. (2000). *Physica B*, **276–278**, 59–62.

Siano, S., Bartoli, L., Santisteban, J. R., Kockelmann, W., Daymond, M. R., De Marinis, G. & Miccio, M. (2006). *Archaeometry*. In the press.

Treimer, W., Strobl, M., Hilger, A., Seifert, C. & Feye-Treimer, U. (2003). *Appl. Phys. Lett.* **83**, 398–400.

Wang, X.-L., Wang, Y. D. & Richardson, J. W. (2002). *J. Appl. Cryst.* **35**, 533–537.

Willis, B. T. M. (1994). *Z. Kristallogr.* **209**, 385–389.